RESEARCH ARTICLE

Nonlinear Shaping in the Picosecond Gap

Randy Lemons[1,2]*, Jack Hirschman[1,2], Hao Zhang[1,2,3], Charles Durfee[4], and Sergio Carbajo[1,2,3]

[1]SLAC National Accelerator Laboratory, Menlo Park, CA 94025, USA. [2]Stanford University, Stanford, CA 94305, USA. [3]University of California, Los Angeles, Los Angeles, CA 90095, USA. [4]Colorado School of Mines, Golden, CO 80401, USA.

*Address correspondence to: rlemons@slac.stanford.edu

Lightwave pulse shaping in the picosecond regime has remained unaddressed because it resides beyond the limits of state-of-the-art techniques, due to either its inherently narrow spectral content or fundamental speed limitations in electronic devices. The so-called picosecond shaping gap hampers progress in all areas correlated with time-modulated light–matter interactions, such as photoelectronics, health and medical technologies, and energy and materials sciences. We report on a novel nonlinear method to simultaneously frequency-convert and adaptably shape the envelope of light wave packets in the picosecond regime by balancing spectral engineering and nonlinear conversion in solid-state nonlinear media, without requiring active devices. We capture computationally the versatility of this methodology across a diverse set of nonlinear conversion chains and initial conditions. We also provide experimental evidence of this framework producing picosecond-shaped, ultranarrowband, near-transform-limited light pulses from broadband, femtosecond input pulses, paving the way toward programmable lightwave shaping at gigahertz-to-terahertz frequencies.

Introduction

Controlling the time-domain intensity shape of ultrashort laser pulses is crucial for various applications in science and technology. Advanced intensity-only modulation in the frequency domain allows for the generation of arbitrary waveforms with controlled amplitude and phase distributions, opening new possibilities for applications in microscopy, time-resolved imaging, laser micromachining, particle acceleration, and attosecond science [1,2]. Managing the temporal characteristics of ultrashort laser pulses has been an active area of development since their inception in the early 1960s. The predominant techniques that have emerged to address this can be broadly classified as either spectral or temporal techniques. Spectral methods specialize in modulating the spectral amplitude and/or phase of broadband optical pulses, typically in the visible to near-infrared (NIR) range, using devices such as spatial-light modulators [3,4] or acousto-optic modulators [5,6] in the Fourier plane of a dispersive element. The main limitation to utilizing spectral methods for pulse shaping is having a sufficient bandwidth for the modulation devices to act upon, resulting in a limitation on input pulse durations on the order of 100 fs or less. Temporal techniques directly modulate the temporal amplitude of pulses most commonly using electro-optic modulators [7,8]. However, the time resolution with direct temporal shaping is limited by the electronic response time of the modulation devices, typically on the order of a nanosecond and above, thus limiting the application of temporal methods to pulses with similar or longer durations. As such, the combined applicable temporal regimes across both methodologies do not include shaping pulses with

transform-limited (TL) durations spanning from a few to hundreds of picoseconds due to the bandwidth of these pulses being too narrow for spectral methods and the duration too short for direct temporal methods.

Achieving efficient control of the spatiotemporal profile of pulses in this region has numerous and immediate applications. For example, certain reactions during photosynthesis have characteristic times on the order of tens of picoseconds [9], potentially opening the door for artificial photosynthesis driven by shaped optical pulses with tens of picosecond duration [10]. The study of photoexcitation and charge carrier dynamics in semiconductors with complex dynamics on the picosecond scale can improve optoelectronic devices for faster information processing [11]. Similarly, new frontiers in ultrafast picosecond-duration electronics [12] can be opened by patterning of picosecond-duration pulses driving nanoplasma excitation [13]. Furthermore, x-ray free-electron lasers (XFELs), the brightest x-ray sources available today, are driven by picosecond-duration photoexcitation laser where the spatiotemporal profile has a drastic impact on the space-space of photoelectrons and thus on the temporal, spatial, and spectral properties of x-ray pulses [14–16].

Successful shaping efforts in this picosecond shaping gap have mainly relied upon stretching femtosecond broadband pulses out to picosecond duration and modulating either the spectral amplitude [17,18] or spectral phase [19,20]. Once the broadband pulses are sufficiently dispersed, the temporal amplitude of the pulse can be roughly approximated by the spectral amplitude profile, allowing for linear mapping of the spectral techniques into the temporal domain. Recently, the

spectral phase transfer technique for temporal pulse shaping has been successfully demonstrated using 4-wave mixing in hollow-core fibers [21–23]. Using the nonlinear optical properties of the fiber enables precise control over the temporal structure of pulses. The desired phase profile can be effectively mapped onto the idler pulse generated through the 4-wave mixing process by injecting a signal pulse with a predefined spectral phase. This approach opens new possibilities for high-precision temporal shaping applications, particularly under high-power regimes. However, its extension to the picosecond regime remains challenging due to transfer efficiency limitations. The difficulty arises from the complex interplay of nonlinear effects and phase-matching conditions required for efficient spectral phase transfer over shorter pulse durations. Alternatively, a shaped pulse can be generated by stacking many copies of few-picosecond-duration pulses with increasing delay and varying amplitude [24]. While these methods are in principle suitable for achieving temporal intensity shaping in the picosecond regime, they exhibit unavoidable downsides in the form of residual spectral chirp or intensity fluctuations due to phase errors. As such, the use of pulses is difficult or impossible in phase-sensitive or intensity-sensitive applications such as nonlinear frequency conversion, micromachining [25], and photoexcitation [16,26,27] where even 5% deviations from expected values can have drastically different measurable results.

Here, we present a broadly applicable and versatile framework with experimental evidence for generating tailored temporal envelopes with (near-)TL spectral bandwidths in the picosecond regime. The baseline operating principle mixes a pair of broadband pulses that have been oppositely chirped with tailored second- and third-order spectral dispersion in a noncollinear sum-frequency generation (SFG) scheme. During the nonlinear interaction, the resultant SFG pulse is generated with a duration commensurate with the stretched duration of the mixed broadband pulses—an intensity envelope that is roughly equal to the sum of the input pulses' envelope in the time domain—and an ultracompressed spectral bandwidth down to the picometer. The bandwidth reduction and summing of opposite spectral chirps result in a pulse that has a remarkably low residual spectral phase noise and fluctuations, thus overcoming the limitations of any prior art. We extend beyond this baseline by adding spectral amplitude shaping onto the mixed input pulses to the SFG in addition to spectral phase control.

Methods

Nonlinear conversion modeling
The dynamics involved with dispersion-controlled nonlinear synthesis (DCNS) include laser propagation, dispersion, and nonlinear conversion in millimeter-scale nonlinear crystals and are described by the one-dimensional nonlinear Schrödinger equation [28,29] (1D-NLSE). To model this, we utilized the symmetrized split-step Fourier method (S-SSFM) [30], which oscillates between the Fourier conjugate domains of time and frequency for calculating nonlinear dynamics and dispersion, respectively, as the numerical method propagates along the crystal. Propagation along the crystal is handled via the angular spectrum method in the spatial frequency domain. Applying the S-SSFM to the 1D-NLSE, the governing equation for our dynamics is given by

$$A(z+dz,t) = \mathcal{F}^{-1}\left[e^{i\frac{C_D}{2}\omega^2 dz} \mathcal{F}\left[e^{iC_{NL}|A|^2 dz} \mathcal{F}^{-1}\left[e^{i\frac{C_D}{2}\omega^2 dz} \mathcal{F}[A(z,t)] \right] \right] \right] \quad (1)$$

where $\mathcal{F}$ and $\mathcal{F}^{-1}$ represent the forward and reverse Fourier transforms, respectively; A describes the pulse envelope in time, t, and space, z; C_D is the dispersion coefficient and governs the linear portion of the equation; and C_{NL} is the nonlinear coefficient. While the linear and nonlinear portions and their effects are not separable a priori, the error generated in handling their effects separately is small as long as the numerical step size, dz, is sufficiently small [29].

Each DCNS scenario was modeled as the interaction between 3 fields, the 2 dispersed input fields and the SFG field, with each being described individually by their respective 1D-NLSE equations. The nonlinear conversion and interfield interactions was handled by the coupled equations for SFG [31],

$$\frac{dA_1}{dz} = \frac{2id_{eff}\omega_1^2}{k_1 c^2} A_2^* A_3 e^{-i\Delta kz} \quad (2a)$$

$$\frac{dA_2}{dz} = \frac{2id_{eff}\omega_2^2}{k_2 c^2} A_1^* A_3 e^{-i\Delta kz} \quad (2b)$$

$$\frac{dA_3}{dz} = \frac{2id_{eff}\omega_3^2}{k_3 c^2} A_1 A_2 e^{i\Delta kz} \quad (2c)$$

where d_{eff} is the effective nonlinearity of the crystal media and Δk is the phase mismatch between the involved fields. Our implementation of the S-SSFM calculated the full envelope of the 3 fields in the time and frequency domains, allowing for explicitly tracking the phase mismatch between each spectral component of each field with respect to the full spectrum of the other 2. As such, the monochromatic plane-wave assumptions underlying the coupled SFG equations are respected.

Results

Theoretical description
Our framework, which we have coined as dispersion-controlled nonlinear synthesis [32], builds on the principle behind spectral compression [33,34] wherein an initial TL broadband—e.g., few-nanometer-bandwidth and beyond in the optical range—pulse is split into 2 identical copies. Here, a substantial amount of equal and opposite second-order dispersion (SOD) is added to the spectral phase of each copy, and then the 2 are mixed in a noncollinear SFG scheme to generate a near-TL picosecond-duration pulse. During SFG, the efficiency of the process is mediated by the wave vector mismatch. For 2 pulses with equal and opposite amounts of spectral chirp, the mismatch can be described by

$$\Delta k = k_1(\omega_1 + \varphi) + k_2(\omega_2 - \varphi) - k_3(\omega_3) \quad (3)$$

where k_i is the wave vector of the frequency components of each field, ω_i is the central frequency, and φ is the variation from ω_i due to spectral chirp. For the special case where the input fields are copies of one another, $\omega_1 = \omega_2$, and thus, for all spectral components, $(\omega_1 + \varphi) + (\omega_1 - \varphi) = 2\omega_1$, resulting in

a TL pulse generated at $2\omega_1$ during SFG [35]. DCNS builds on these principles by adding third-order dispersion (TOD) to the baseline SOD when modifying the spectral phase and spectral amplitude shaping before nonlinear conversion. Unlike SOD, the added per-pulse TOD and spectral filtering are not held to the equal and opposite requirement like SOD. In theory, the SOD could also be adjusted individually; however, the nonlinear conversion efficiency is quickly decreased as the SODs of pulse pair become mismatched [35]. By including these 2 shaping factors for the 2 incident pulses, we add 4 additional degrees of freedom for shaping the temporal intensity profile of the SFG pulse, drastically increasing the effective parameter space. For each pulse, the applied spectral phase is then a combination of both SOD (φ_2) and TOD (φ_3), where φ_2 is the primary control on pulse duration and φ_3 controls the final SFG pulse envelope shape. However, if the applied φ_2 is increased to generate a longer SFG pulse, TOD must also increase to maintain the desired shape. This relationship is linear, and by defining the ratio between TOD and SOD, $\alpha = \varphi_3 / \varphi_2$, the envelope duration and shape for a given input bandwidth can be described by φ_2 and α.

To generate a narrowband SFG pulse with the desired shape, there are 2 main considerations when determining the sign and magnitude of the applied phases. First, to maintain the narrowband generation requirement during SFG, the 2 pulses must have equal and opposite amounts of φ_2. The magnitude of φ_2 is given by solving

$$\Delta t = t_0 \sqrt{1 + \left(4\ln2\frac{\varphi_2}{t_0^2}\right)^2} \qquad (4)$$

for φ_2, where Δt is the final desired duration and t is the TL input duration. This equation comes from the electric field for a TL Gaussian pulse after acquiring a fixed amount of SOD given by

$$E(\omega) = \sqrt{A_\omega}\, e^{-\ln2\frac{4(\omega-\omega_0)^2}{\Delta\omega^2}}\, e^{i\varphi_2\frac{(\omega-\omega_0)^2}{2}} \qquad (5)$$

where A is the spectral amplitude. By Fourier transforming this equation to the time domain and squaring it to obtain the intensity, the relation above relating stretched duration to input parameters can be extracted [36]. Second, the sign and magnitude of φ_3 are allowed to vary based on the desired SFG temporal envelope shape. Imparting the 2 copies with equal magnitude and opposite sign φ_3 results in symmetric profiles while allowing either sign or magnitude to vary results in asymmetric ones. While the absolute magnitudes of the imparted phases are dependent on input bandwidth and desired shaping, a larger α implies a more substantial degree of shaping and a greater departure from the input pulse shapes.

In Fig. 1, we showcase a selection of shaping possibilities with phase-only DCNS to exemplify the capabilities of this method. For each case, the shown intensity envelopes are after applying a 0.5-nm super-Gaussian spectral filter centered on the central frequency of the SFG to quench high-frequency oscillations inherent to the mixing process (Supplementary Materials). The 4 scenarios that we present are (a) square-wave, (b) triangular, (c) double-hump, and (d) linear-ramp intensity distributions. Each scenario uses an input pulse with different central wavelength and bandwidth to illustrate the applicability of DCNS to a wide range of laser systems. Of particular note

are the triangular and double-hump cases for their direct applicability to high acceleration gradients in plasma wakefield acceleration [37] and emittance reduction in XFEL facilities, respectively [15,38]. For the triangular case, the nonsymmetric shape was achieved by having the same sign and magnitude of φ_3, and therefore opposite signed α's, on the 2 copies of the input. By having the same sign, the characteristic third-order temporal tails are aligned on the same side of the main peak. In the shown example, the pulse starts with a large intensity spike, potentially useful for driving optical shock waves, but by flipping the sign of both inputs, the temporal trace can be reversed in time to resemble a gradual ramp. However, any asymmetry generated this way also results in a residual phase on the SFG pulse, potentially limiting the use of these pulses to non-phase-sensitive applications. In the double-hump scenario, the 2 inputs are functionally identical to the square wave with equal and opposite φ_2 and φ_3 but each has been shifted by 10 ps in time relative to the other to generate an intensity void. These examples are a small subset of potentially achievable temporal profiles given the large parameter ranges of φ_2, φ_3, time delay, and input pulse properties and serve to illustrate the flexibility behind DCNS rather than limit potential application.

Experimental phase-only DCNS

To experimentally verify DCNS, we generated a near-TL 20-ps flattop pulse in ultraviolet (UV) from a commercial Yb:KGW laser system producing 250-fs pulses centered at a wavelength of 1,024 nm. Full details of this laser system can be found in Note S1. To generate this temporal pulse profile, the required SOD and TOD applied to each pulse are ±2.561 ps^2 and ∓0.28 ps^3, respectively, corresponding to an $\alpha = -0.11$ ps. The desired temporal intensity profile of the SFG after a 0.5-nm bandpass filter is shown in Fig. 1B. This shape is similar to a higher-order super-Gaussian pulse with a flat plateau across the central region of the pulse with rise and fall times of approximately 4 ps. These characteristics are highly sought after for reducing the emittance of photoemission-based free-electron sources for ultrafast electron microscopy, high-energy physics, XFELs, and other secondary radiation sources.

Our experimental layout (Fig. 2) is divided into 2 main areas: spectral phase manipulation and nonlinear conversion. The phase manipulation portion is responsible for splitting the NIR input pulse into 2 distinct but equal copies, referred to as the stretcher and compressor pulses, and applying the equal and opposite spectral phases. For our input parameters, achieving $\alpha \sim 0.11$ with this magnitude of SOD is a nontrivial task and unachievable within a single dispersive device utilizing gratings or prisms. We avoid this limitation by combining a matched grating compressor and stretcher designed to impart substantially more SOD than desired and the proper amount of TOD with a chirped volume Bragg grating (CVBG) designed to compensate for the residual SOD of both devices. After splitting the stretcher and compressor, pulses are sent through the respective single grating devices and then reflected by opposite ends of the CVBG to realize the ±2.561 ps^2 SOD and ∓0.28 ps^3 TOD. It is important to note that the layout we have chosen for our experimental demonstration is not the only viable layout for DCNS as a framework. More sophisticated methods for manipulating the individual phase of the input pulses could be conceptualized. Examples of such solutions are distinct synchronized laser systems or pulse arrays, individualized spatial-light modulators or acousto-optic modulators for the inputs,
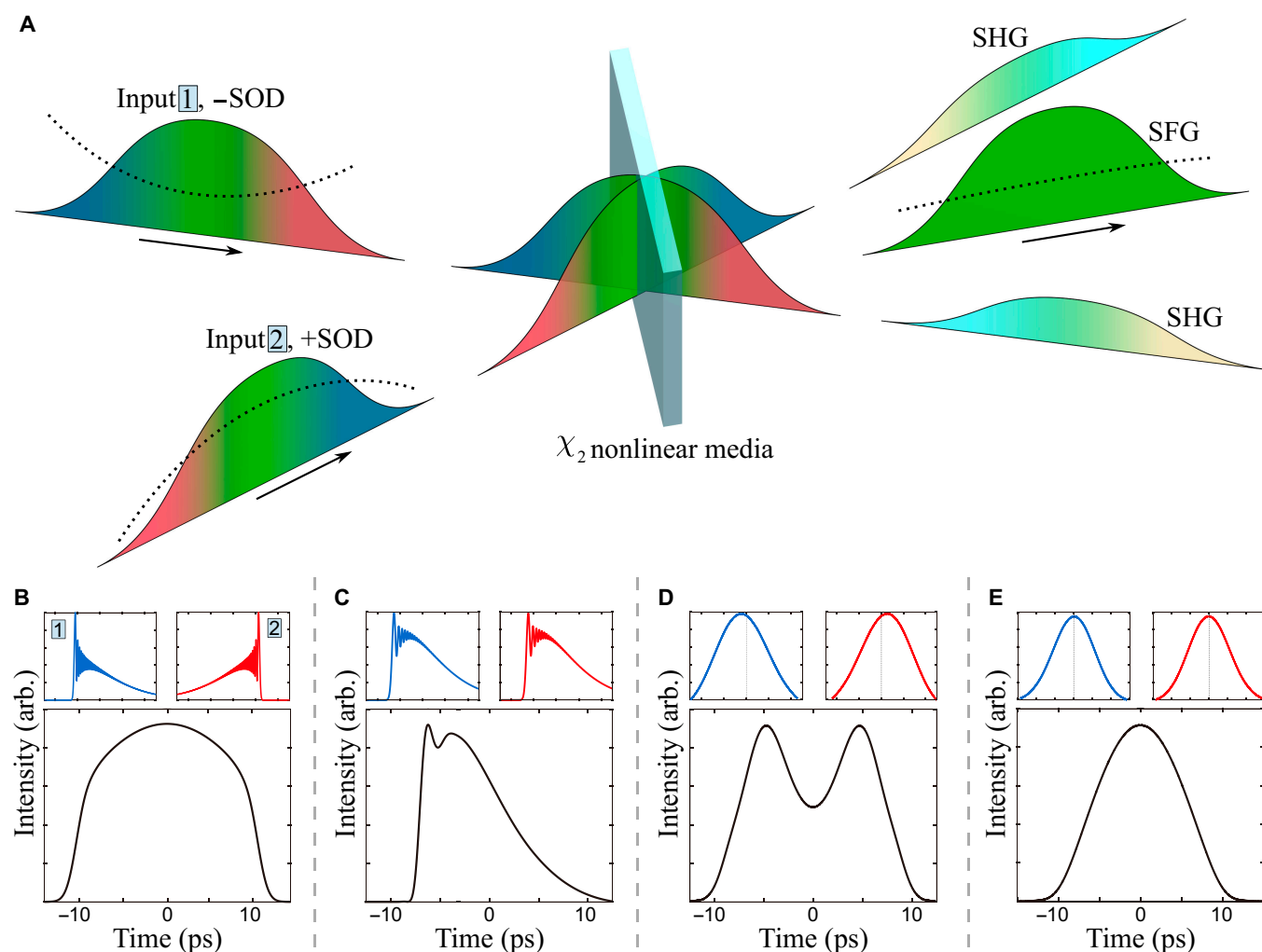
Fig. 1. (A) Conceptual representation of dispersion-controlled nonlinear synthesis (DCNS) where 2 oppositely chirped broadband pulses (phase represented with dashed lines) are incident on a χ_2 nonlinear media. Two broadband chirped parasitic second-harmonic-generation (SHG) pulses are generated along the same direction as the inputs, and a narrowband near-transform-limited (near-TL) sum-frequency generation (SFG) pulse is generated at the mid-angle. (B to E) Four potential nonlinear shaping examples of the narrowband pulse via phase-only DCNS with varying second-order dispersion (SOD) and third-order dispersion (TOD) after a spectral bandpass filter of 0.5 nm. The temporal intensity profiles of input 1 and input 2 are shown in blue and red, respectively. The chosen shapes are included to demonstrate the flexibility of the method to input parameters and final result. For more information on input pulse parameters and the applied spectral phase, see Table S1.
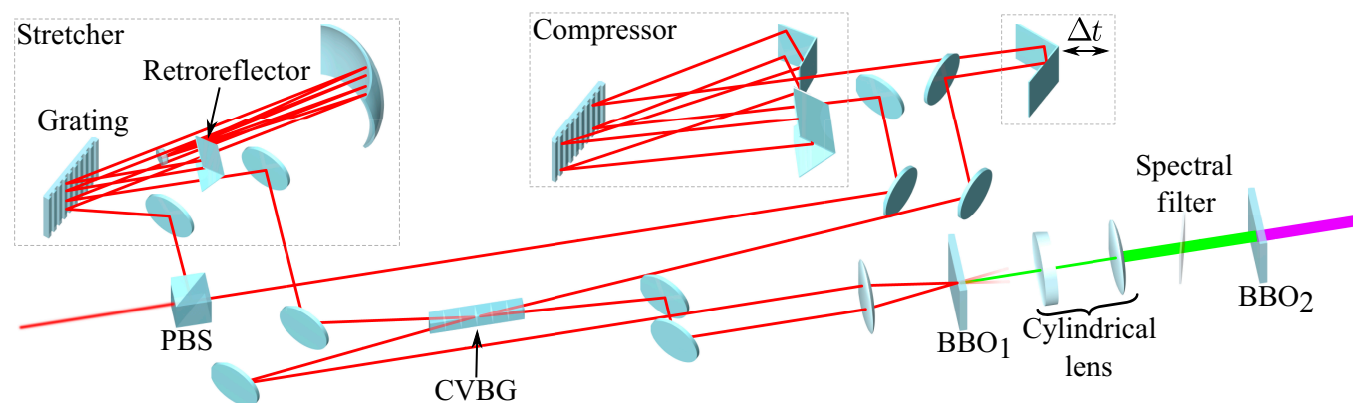

Fig. 2. Experimental layout of phase shaping and nonlinear conversion elements used for generating a flattop in ultraviolet (UV). A single input beam is split via a polarizing beam splitter (PBS) with equal parts going through the grating stretcher and grating compressor. Each beam is then sent into opposite ends of the chirped volume Bragg grating (CVBG), reflected internally, and finally overlapped in BBO_1 for SFG. Temporal overlap in BBO_1 is achieved through a horizontal retroreflector on a linear delay stage (Δt). The SFG beam travels through a cylindrical lens set, and a spectral filter and is then converted to UV in BBO_2. BBO, β-barium borate.

or even mixing pulses from 2 separate amplification systems from the same master oscillator. Ultimately, manipulation of SOD, TOD, and spectral filtering on a per-pulse basis is all that is required for DCNS.

After phase manipulation, the 2 pulses are sent through the nonlinear conversion chain in which the SFG pulse is generated, frequency-filtered, and further converted to the fourth harmonic of the NIR input. Each nonlinear conversion step is done in a critically phase-matched β-barium borate (BBO) crystal. In the SFG step, the 2 pulses are made collinear and horizontally separated and then focused by a single lens onto a 2-mm BBO at an angle of 1.5° to each other. Time overlap is achieved with a horizontal retroreflecting delay stage in the compressor beam path. Although both NIR inputs are spatially Gaussian with no ellipticity, the SFG beam is generated with a moderate ellipticity due to the crossing angle inside the crystal. After the residual NIR and parasitic second-harmonic-generation pulses are discarded, this ellipticity is corrected by passing the SFG pulse through a cylindrical lens before spectral filtering. The spectral filter is angle-tuned so that the center wavelength of the filter is the same as the SFG pulse. While a direct measurement of the SFG pulse's temporal intensity profile was not performed in this study, the narrowband characteristics and flat-phase properties of the SFG pulse ensure the preservation of its temporal profile through subsequent nonlinear conversion stages. Therefore, the SFG pulse is converted to the fourth harmonic of the NIR via degenerate collinear second harmonic generation in a 3-mm BBO where the temporal intensity profile is measured.

The UV temporal profile is measured via third-harmonic cross-correlation with a 70-fs, 1,035-nm pulse from the oscillator feeding the main laser amplifier. In Fig. 3A, the initial temporal profile of the UV from the above setup is shown. While this profile does demonstrate the sharp rise and fall times that were seen in the simulation, the flat central region exhibits noticeable intensity modulations. These modulations originated from an imperfection in the CVBG that removed a small amount of the long-wavelength side of the stretcher and compressor pulses. This loss of information resulted in an unbalanced contribution of the short wavelengths and thus higher-frequency oscillations across the temporal profile. To correct this, we inserted a long-pass filter before the SFG focusing lens to remove a small amount of the short-wavelength side of the NIR inputs. Once the spectrum of the inputs was symmetrized, the resulting UV profile (Fig. 3B) drastically smoothed across the central region while maintaining the sharp rise and fall times as desired. Additionally, peak intensity can be shifted in time (Fig. 3C to F) throughout the pulse by only varying the relative energy of the 2 input pulses with respect to one another. In this case, the peak intensity naturally shifts in time toward the more intense input pulse, allowing for another degree of freedom in shaping the final pulse. From the baseline flattop shape (Fig. 3B), the rising and falling edge can be preferentially enhanced in a continuous fashion as shown in the series (Fig. 3).

Experimental phase and amplitude DCNS shaping

Affecting the UV pulse shape in this way revealed an important extension of the DCNS process toward arbitrary pulse shaping:
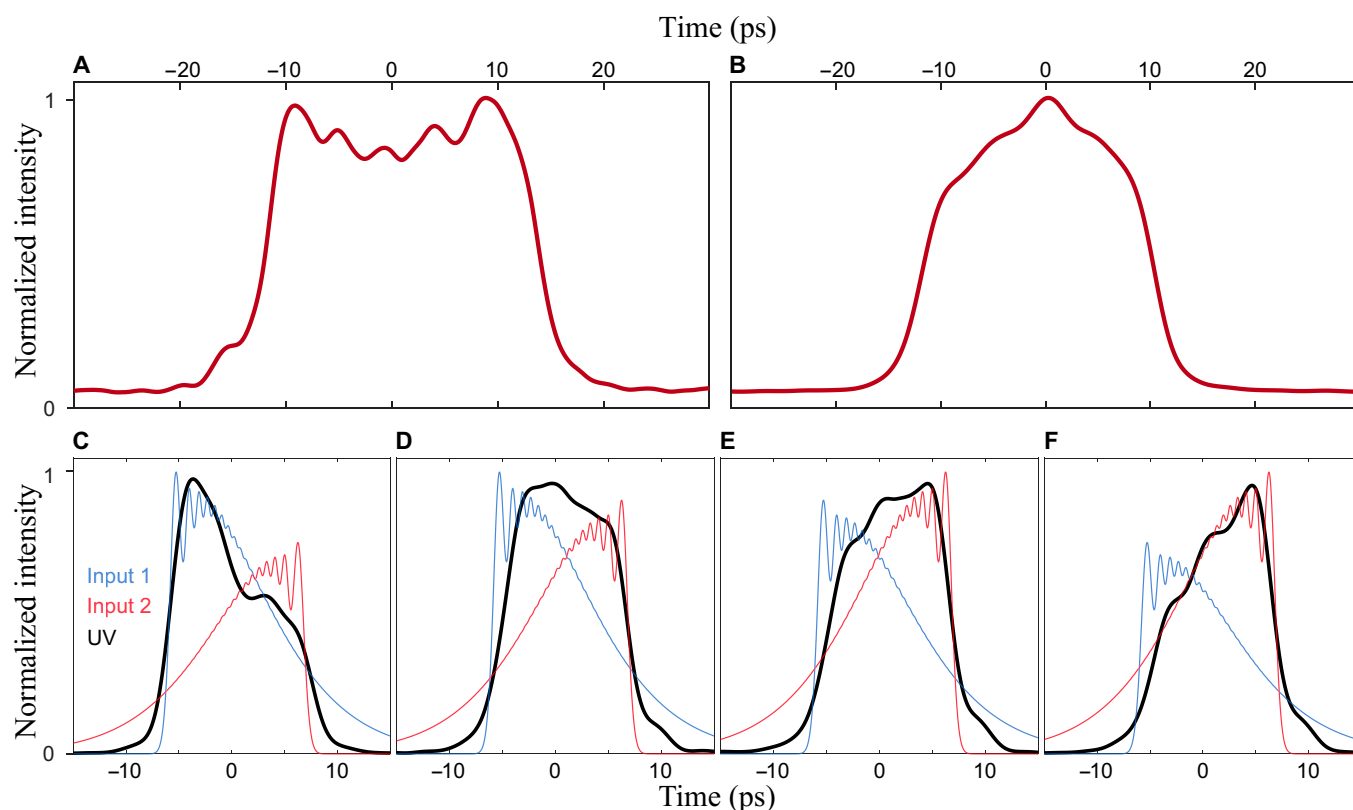
Fig. 3. UV temporal intensity profile (A) without infrared (IR) filtering and (B) with IR filtering. IR filtering is used to symmetrize the spectrum of both inputs post-interaction with the CVBG. (C to F) Once the spectrum is symmetrized, power can be shifted along the UV pulse (black) by adjusting the relative amplitudes of IR inputs 1 (blue) and 2 (red). IR input profiles are simulated from the expected spectral phase after the stretcher/compressor and CVBG.

programmable spectral amplitude filtering. In Fig. 4, we illustrate the potential of applying amplitude masking on top of a DCNS-shaped pulse. In this example, 2 scenarios of spectral holes being applied to the pulse with negative SOD before SFG were investigated: 2 spectral holes each ±1.5 nm away from the central wavelength with widths of 0.5 nm (Fig. 4, left), and a single spectral hole with a 1-nm width at the central wavelength of the pulse (Fig. 4, right). Figure 4A and B are simulated results of applying these 2 filters to the flattop baseline DCNS pulse, and Fig. 4C and D are experimental demonstrations of the same spectral filters. In the case of the double hole, the envelope develops a strong intensity modulation across the central peak flanked by 2 small pre- and postpulses. For the single spectral hole, the SFG pulse has a temporal profile with a deep central valley and sharply rising triangular side lobes. Experimentally, both cases are well matched in qualitative shape with the double hole generating the trimodulated central peak with flanking subpulses and the single spectral hole generating the double-peaked pulse. While the experimentally generated pulses have the same qualitative shape, they are slightly longer than the simulated results. This deviation likely derives from the greater SOD and α from the matched grating pair than the SOD and α in simulation.

For both of these cases, intensity is reduced but does not go to zero at temporal locations corresponding to the location of the holes within the spectrum. While the SOD applied to these pulses is substantial, especially when discussing ultrashort optics, each frequency component still temporally overlaps with those around it by some amount. As such, there is still some power within the temporal region from frequency components that have not been filtered out. Should the magnitude

of the applied SOD grow, the mapping of spectrum to time becomes closer to one-to-one and the shaping more precise. However, this effect is muted by the spatial overlap and lack of perfect spectral filters in the Fourier plane of the compressor grating where the spectral filtering is applied. Lastly, like the baseline flattop scenario, these temporal traces are collected from the upconverted UV pulse rather than directly after SFG, indicating that even with spectral shaping, the SFG pulse maintains its narrowband, flat-phase nature. An intrinsic limitation of spectral amplitude shaping is decreasing the input pulse energy to such a degree that efficient nonlinear conversion in the SFG stage is no longer possible. However, by combining this with phase-only DCNS, the degree of potential shaping is extended beyond what can be achieved in shaping methods relying solely on amplitude masking for high-energy or high-average-power applications.

Discussion

We have described and demonstrated DCNS, a new methodology that can generate pulses with tailored temporal envelope shapes in the picosecond range. By utilizing noncollinear SFG with oppositely chirped inputs, we avoid the pitfalls of previous methods, such as residual spectral chirp, phase discontinuities, or unwanted intensity fluctuations, while integrating the spectral phase and amplitude shaping to enable the flexibility of achievable temporal intensity profiles. As a proof-of-principle experiment based on this framework, we generated a 20-ps temporally flattop UV pulse with little intensity fluctuations and a highly compressed spectral bandwidth from 240-fs 1,024-nm inputs. Additionally, we demonstrated a potential avenue toward
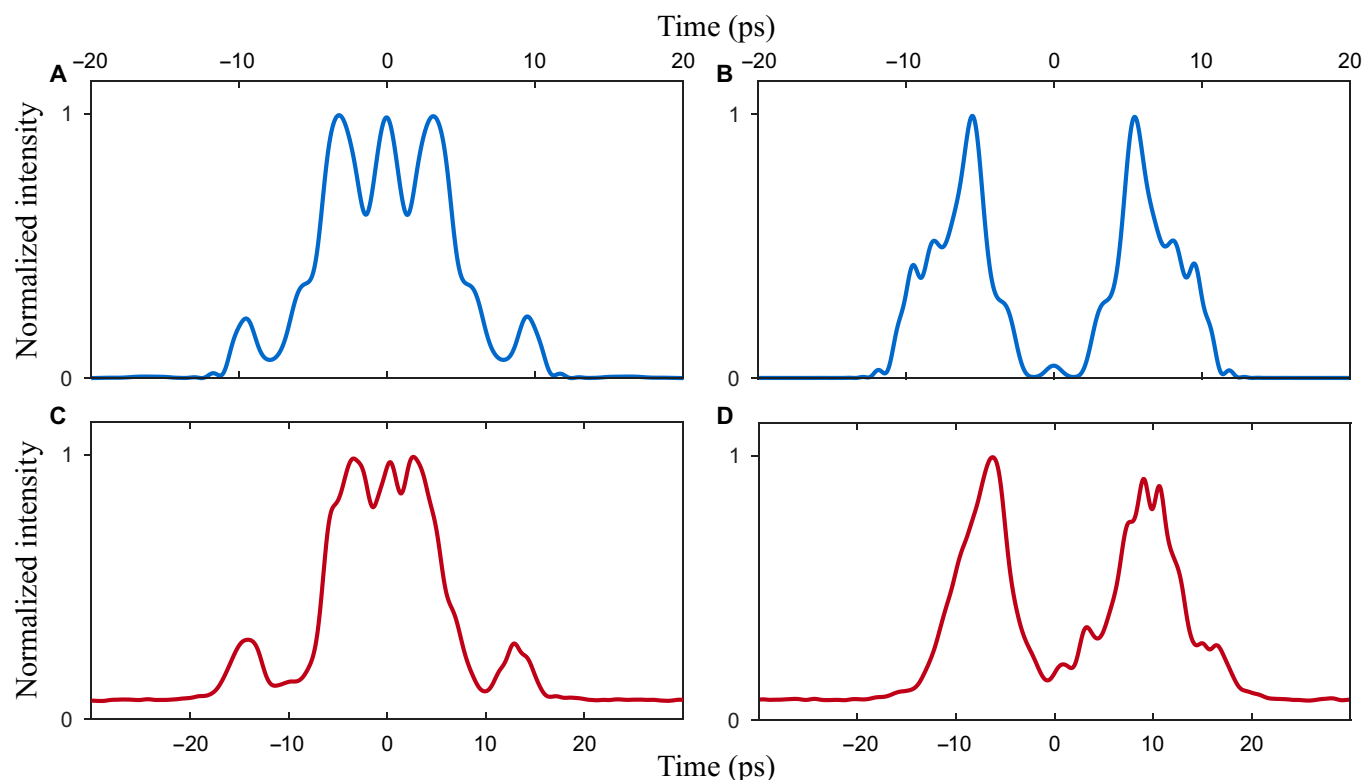
Fig. 4. Simulation of direct temporal intensity shaping during DCNS due to spectral amplitude shaping of an input pulse with (A) 2 spectral holes, one on either side of the central frequency and (B) a single spectral hole at the central frequency. Experimental spectral amplitude shaping for the (C) 2 spectral holes, one on either side of the central frequency and (D) a single spectral hole at the central frequency.

adaptive temporal shaping through spectral amplitude modification of the broadband inputs before nonlinear conversion. Our experimental implementation of DCNS is only one of many potential solutions with the most immediate improvements being found by eliminating the requirement of a CVBG for correcting large amounts of SOD. Furthermore, as our method is mediated by nonlinear frequency conversion, it is naturally limited to applications where the initial spectral region is not the one of interest. The mediation by nonlinear conversion also places limitations on the amount of stretching that can be achieved. Although there is nothing in our method intrinsically limiting the final stretched duration, if the applied phase is too high, then the pulse intensity will drop to such a level that SFG can no longer be obtained. This can be compensated to some extent by tighter focusing or higher pulse energies up to the point of damage. As our method uses phase as means for pulse shaping during nonlinear conversion, it is limited by the principles of the underlying processes. Ultimately, by circumventing the limitations of prior attempts at bridging the picosecond shaping gap, our method is readily deployable for a plethora of applications such as patterning of picosecond-duration pulses driving nanoplasma excitation, enhancement of ultrafast photoelectron sources such as XFELs, and laser-driven artificial photosynthesis.

Acknowledgments

Data Availability

The data that support the findings of this study are available from the corresponding author upon reasonable request.

Supplementary Materials

Table S1
Notes S1 and S2

References

1. Bejot P, Kibler B. Taming light in all dimensions. *Nat Photonics*. 2022;16:671–672.

2. Forbes A, De Oliveira M, Dennis MR. Structured light. *Nat Photonics*. 2021;15:253–262.

3. Mironov SY, Potemkin A, Gacheva E, Andrianov AV, Zelenogorskii VV, Krasilnikov M, Stephan F, Khazanov EA. Shaping of cylindrical and 3D ellipsoidal beams 311 for electron photoinjector laser drivers. *Appl Opt*. 2016;55(7):1630–1635.

4. Penco G, Allaria E, Badano L, Cinquegrana P, Craievich P, Danailov M, Demidovich A, Ivanov R, Lutman A, Rumiz L, et al. Optimization of a high brightness photoinjector for a 313 seeded FEL facility. *J Instrum*. 2013;8:P05015.

5. Li Y, Chemerisov S, Lewellen J. Laser pulse shaping for generating uniform three-dimensional ellipsoidal electron beams. *Phys Rev Spe Top Accel Beams*. 2009;12(2):Article 020702.

6. Petrarca M, Musumeci P, Mattioli M, Vicario C, Gatti G, Ghigo A, Cialdi S, Boscolo B. Production of temporally flat top UV laser pulses for SPARC photo-injector. Paper presented at: International Conference on Charged and Neutral Particles Channeling Phenomena II; 2006 Jul 3–7; Rome, Italy.

7. Diels J-C, Rudolph W. In: *Ultrashort laser pulse phenomena*. 2nd ed. Burlington (MA): Academic Press; 2006. Chapter 8, Pulse shaping; p. 433–556.

8. Skeldon MD. Optical pulse-shaping system based on an electro-optic modulator driven by an aperture-coupled-stripline electrical-waveform generator. *J Opt Soc Am B*. 2002;19(10):2423–2426.

9. Guo Y, He L, Ding Y, Kloo L, Pantazis DA, Messinger J, Sun L. Closing Kok's cycle of nature's water oxidation catalysis. *Nat Commun*. 2024;15:5982.

10. Baikie TK, Wey LT, Lawrence JM, Medipally H, Reisner E, Nowaczyk MM, Friend RH, Howe CJ, Schnedermann C, Rao A, et al. Photosynthesis re-wired on the pico-second timescale. *Nature*. 2023;615(7954):836–840.

11. Perez C, Ellis SR, Alcorn FM, Smoll EJ, Fuller EJ, Leonard F, Chandler D, Talin AA, Bisht RS, Ramanathan S, et al. Picosecond carrier dynamics in InAs and GaAs revealed by ultrafast electron microscopy. *Sci Adv*. 2024;10(20):eadn8980.

12. Samizadeh Nikoo M, Jafari A, Perera N, Zhu M, Santoruvo G, Matioli E. Nanoplasma enabled picosecond switches for ultrafast electronics. *Nature*. 2020;579:534–539.

13. Sun F, Qu Q, Li H, Jiang S, Liu Q, Ben S, Pei Y, Liang J, Wang J, Song S, et al. All-optical steering on the proton emission in laser-induced nanoplasmas. *Nat Commun*. 2024;15:5150.

14. Zhou F, Ben-Zvi I, Babzien M, Chang XY, Doyuran A, Malone R, Wang XJ, Yakimenko V. Experimental characterization of emittance growth induced by the nonuniform transverse laser distribution in a photoinjector. *Phys Rev Accel Beams*. 2002;5(9):094203.

15. Penco G, Danailov M, Demidovich A, Allaria E, de Ninno G, di Mitri S, Fawley WM, Ferrari E, Giannessi L, Trovó M. Experimental demonstration of electron longitudinal phase-space linearization by shaping the photoinjector laser pulse. *Phys Rev Lett*. 2014;112(4):Article 044801.

16. Zhang H, Gilevich S, Miahnahri A, Alverson SC, Brachmann A, Duris J, Franz P, Fry A, Hirschman J, Larsen K, et al. The Linac Coherent Light Source II photoinjector laser infrastructure. *High Power Laser Sci Eng*. 2024;12:Article e51.

17. Agostinelli J, Harvey G, Stone T, Gabel C. Optical pulse shaping with a grating pair. *Appl Opt*. 1979;18(14):2500–2504.

18. Haner M, Warren WS. Generation of arbitrarily shaped picosecond optical pulses using an integrated electrooptic waveguide modulator. *Appl Opt*. 1987;26(17):3687–3694.

19. Zhang BM, Feng Y, Lin D, Price JHV, Nilsson J, Alam S, Shum PP, Payne DN, Richardson DJ. Demonstration of arbitrary temporal shaping of picosecond pulses in a radially polarized Yb-fiber MOPA with > 10 W average power. *Opt Express*. 2017;25(13):15402–15413.

20. Weiner AM, Heritage JP, Kirschner EM. High-resolution femtosecond pulse shaping. *J Opt Soc Am B*. 1988;5(8): 1563–1572.

21. Zuo P, Fuji T, Suzuki T. Spectral phase transfer to ultrashort UV pulses through four-wave mixing. *Opt Express*. 2010;18(15):16183–16192.

22. Siqueira J, Mendonca CR, Zilio SC, Misoguti L. Spectral phase transfer from near IR to deep UV by broadband phase-matched four-wave mixing in an argon-filled hollow core waveguide. *J Phys B Atomic Mol Phys*. 2016;49(19): Article 195601.

23. Zhang H, Sun LS, Hirschman J, Shariatdoust MS, Belli F, Carbajo S. Optimizing spectral phase transfer in four-wave mixing with gas-filled capillaries. *Opt Express*. 2024;32(25):44397–44412.

24. Will I, Klemz G. Generation of flat-top picosecond pulses by coherent pulse stacking in a multicrystal birefringent filter. *Opt Express*. 2008;16(19):14922–14937.

25. Jiang K, Zhang P, Song S, Sun T, Chen Y, Shi H, Yan H, Lu Q, Chen G. A review of ultra-short pulse laser micromachining of wide bandgap semiconductor materials: SiC and GaN. *Mater Sci Semicond Process*. 2024;180:Article 108559.

26. Bettoni S, Divall MC, Ganter R, Pedrozzi M, Prat E, Reiche S, Schietinger T, Trisorio A, Vicario C, Goryashko V. Impact of laser stacking and photocathode materials on microbunching instability in photoinjectors. *Phys Rev Accel Beams*. 2020;23(2):Article 024401.

27. Mitchell C, Emma P, Qiang J, Venturini M. Sensitivity of the microbunching instability to irregularities in cathode current in the LCLS-II beam delivery system. Paper presented at: 2nd North American Particle Accelerator Conference (NAPAC2016); 2016 Oct 9–14; Chicago, IL.

28. Karjanto N. The nonlinear Schrödinger equation: A mathematical model with its wide-ranging applications. arXiv. 2019. https://arxiv.org/abs/1912.10683

29. Agrawal GP. Nonlinear fiber optics. In: Christiansen PL, Sørensen MP, Scott AC, editors. *Nonlinear science at the dawn of the 21st century*. Berlin (Germany): Springer; 2000. p. 195–211.

30. Weideman J, Herbst BM. Split-step methods for the solution of the nonlinear Schrödinger equation. *SIAM J Numer Anal*. 1986;23(3):485–507.

31. Boyd RW. *Nonlinear optics* Amsterdam: (the Netherlands): Academic Press; 2019.

32. Lemons R, Neveu N, Duris J, Marinelli A, Durfee C, Carbajo S. Temporal shaping of narrow-band picosecond pulses via noncolinear sum-frequency mixing of dispersion-controlled pulses. *Phys Rev Accel Beams*. 2022;25(1):Article 013401.

33. Raoult F, Boscheron A, Husson D, Sauteret C, Modena A, Malka V, Dorchies F, Migus A. Efficient generation of narrow-bandwidth picosecond pulses by frequency doubling of femtosecond chirped pulses. *Opt Lett*. 1998;23(14):1117–1119.

34. Ribeyre X, Rouyer C, Raoult F, Husson D, Sauteret C, Migus A. All-optical programmable shaping of narrow-band nanosecond pulses with picosecond accuracy by use of adapted chirps and quadratic nonlinearities. *Opt Lett*. 2001;26(15):1173–1175.

35. Kuzmin I, Mironov SY, Martyanov M, Potemkin A, Khazanov E. Highly efficient fourth harmonic generation of broadband laser pulses retaining 3D pulse shape. *Appl Opt*. 2021;60(11):3128–3135.

36. Siegman AE. *Lasers* Mill Valley (CA): University Science Books; 1986.

37. Tan WH, Piot P, Zholents A. Formation of temporally shaped electron bunches for beam driven collinear wakefield accelerators. *Phys Rev Accel Beams*. 2021;24(5):Article 051303.

38. Dowell DH. Sources of emittance in RF photocathode injectors: Intrinsic emittance, space charge forces due to non-uniformities, RF and solenoid effects. arXiv. 2016. https://arxiv.org/abs/1610.01242